J. Fluid Mech. (2019), *vol.* 861, *pp.* 180–199.
doi:10.1017/jfm.2018.859

A flow separation model for hydrofoil, propeller and duct sections with blunt trailing edges

Weikang Du[1,†] **and Spyros A. Kinnas**[1]

[1]Ocean Engineering Group, Department of Civil, Architecture and Environmental Engineering, University of Texas at Austin, Texas, TX 78712, USA

(Received 22 December 2017; revised 11 October 2018; accepted 22 October 2018; first published online 19 December 2018)

The panel method does not apply to hydrofoils, propellers and ducts with blunt trailing edges due to the flow separation downstream. In this paper, a model is proposed to represent the flow separation with an extension, and a low-order panel method coupled with a boundary layer solver is used. The criteria of zero lift and zero moment are adopted to determine the end of the extension zone, and flow separation criteria are used to determine the starting points on either side of the section. The model is applied to hydrofoil, bare duct and ducted propeller sections with blunt trailing edges. The pressure distributions and skin frictions along the hydrofoils and ducts correlate well with those from the Reynolds-averaged Navier–Stokes method. The thrust and torque of the propeller agree much better with experimental measurements when the extension is determined from this model rather than choosing random locations. This model requires much less computational effort while preserving high accuracy, and thus can be used reliably in designing and analysing hydrofoils and propeller ducts with blunt trailing edges.

Key words: boundary layer separation, computational methods

1. Introduction

The analysis of ducted propellers is a non-trivial task due to the complex flow interaction between the propeller and the duct. In the past, many attempts have been made worldwide and their methodologies can be categorized as (i) the vortex lattice method (VLM) on the propeller and the boundary element method (BEM, more commonly known as the panel method) on the duct (Kerwin *et al.* 1987), (ii) the BEM on both the propeller and the duct (Lee & Kinnas 2006), (iii) the Reynolds-averaged Navier–Stokes (RANS) method on the duct and the BEM or the VLM on the propeller (Kerwin *et al.* 1994; Bosschers *et al.* 2015; Su & Kinnas 2017) and (iv) the RANS method on both the propeller and the duct (Hoekstra 2006; Majdfar *et al.* 2017).

In the RANS method, the flow separation can be captured, so the last two methods are applicable to ducts with blunt trailing edges (TEs). However, up to now the simulation cost for the RANS method has been relatively high, not to mention the time for meshing (with high-resolution grids to reveal the details of the flow field, as

† Email address for correspondence: allendu1988@utexas.edu

in the boundary layer or after TEs) and post-processing, thus more efficient tools are needed for the ducted propellers, especially in the design stage.

These needs are routinely satisfied by the VLM and the BEM, which are based on the potential theory and widely used in the daily design practice of open and ducted propellers due to their high efficiency and acceptable accuracy (Moulijn 2015). By an empirical drag-to-lift coefficient (Kerwin & Lee 1978) or by coupling the VLM or BEM with a two-dimensional boundary layer integral equation solver (the viscous/inviscid interaction method, or VII) (Drela 1989; Kinnas *et al.* 2007), the effect of the viscosity can be considered. Compared with the VLM, the panel method can handle the propeller geometries more precisely, and thus has become increasingly popular.

Tian & Kinnas (2012) showed that a proper wake alignment model can improve the accuracy of the predicted propeller performance in the panel method, especially at low advanced ratios and, therefore, introduced a pseudo-unsteady wake alignment scheme (full wake alignment scheme, or FWA). Kinnas, Fan & Tian (2015) and Kim, Kinnas & Du (2018) extended this scheme for ducted propellers by including the duct-induced velocities in the FWA. Similar approaches were adopted by Baltazar, de Campos & Bosschers (2012), who used a rudimentary method to take into account the boundary layer over the duct inner surface by assuming a power law velocity profile and reduced the pitch of the blade wake near the tip.

The panel method only applies to hydrofoil, propeller and duct sections with sharp TEs due to lack of proper models for the flow separation downstream. However, blunt TEs are commonly seen in real propellers and ducts for structural reasons or to reduce the high-pitched noises (often referred to as the singing edges). On the other hand, the duct trailing wake has a strong impact on the propeller open water characteristics, i.e. thrust, torque and efficiency, thus how to handle the wake after a blunt TE with the panel method is of practical significance. Bosschers *et al.* (2015) specified a chord-wise location on the duct with a blunt TE for panels adjacent to the trailing wake and assumed a constant pressure distribution downstream due to the flow separation. For the same duct section, Moulijn (2015) modified the blunt TE to sharp TE with a straight line by specifying a radial position and it is shown that by adjusting this position, the ducted propeller characteristics predicted by the panel method can match the experimental measurements. Moulijn's (2015) study showed the importance of correctly handling the duct trailing wake but did not provide a self-sufficient method for ducted propellers with blunt TEs.

The flow separation after the blunt TEs has been studied either theoretically (Surana, Grunberg & Haller 2006) or experimentally (Magi & Gai 1998), and has been used to reduce drag or vibrations (Greenway & Wood 1973; Park *et al.* 2006). Pan & Kinnas (2011) applied an extension model and the VII approach to predict the performance of hydrofoils and propellers with non-zero thickness TEs, where the extension started from the two sharp corners of the TE. In the present work, an improved extension model is proposed to represent the local flow separation downstream of blunt TEs in hydrofoils and propeller ducts. The flow is assumed to be incompressible, fully wetted and steady, i.e. without any cavitation or vortex shedding (only the mean flow is considered). To make the conclusions from the presented method applicable to full-scale ducted propellers with blunt TEs, the flow is also assumed to be fully turbulent. In the VII method, the distances from the transition points to the leading edge of the foil or duct are forced to be 1 % of the chord length, and correspondingly, results are compared with those from fully turbulent RANS simulations. Based on the boundary layer equations, it is assumed that the pressure is constant in the separated region,

which leads to the criteria of zero lift and zero moment. A low-order panel method coupled with a boundary layer solver is applied, and the separation points, where the skin friction becomes equal to zero (Servini, Smith & Rothmayer 2017), are used to determine the locations at which to start the extension in an iterative manner. In the ducted propeller case, a Wageningen propeller (Ka series) operating with a blunt TE duct are solved in the extension model with a full wake alignment scheme so that the performance and pressure on the duct are predicted accurately. Results from this model are compared either with those from the steady RANS simulations or with experimental measurements.

2. Numerical method

2.1. *The viscous/inviscid interaction (VII) method*

In the panel method, the total flow velocity $\boldsymbol{q}$ is decomposed into an incoming flow $\boldsymbol{q}_{in}$ and a propeller-induced flow $\boldsymbol{U}_{ind}$ (the perturbation velocity),

$$\boldsymbol{q} = \boldsymbol{q}_{in} + \boldsymbol{U}_{ind}. \tag{2.1}$$

$\boldsymbol{U}_{ind}$ can be treated as the potential flow which is governed by the Laplace equation

$$\boldsymbol{U}_{ind} = \nabla\phi, \quad \nabla^2\phi = 0, \tag{2.2a,b}$$

where ϕ is the perturbation potential.

The Kutta condition is required which means the velocity must remain finite

$$|\nabla\phi| < \infty \quad \text{at the trailing edge.} \tag{2.3}$$

By using Green's identity, equation (2.2) can be written in the boundary integrated form:

$$2\pi\phi_p = \iint_{S_H} \left[\phi_p \frac{\partial G(p,p')}{\partial \boldsymbol{n}_{p'}} - G(p,p')\frac{\partial \phi_p}{\partial \boldsymbol{n}_{p'}}\right] \mathrm{d}S + \iint_{S_W} \Delta\phi_W \frac{\partial G(p,p')}{\partial \boldsymbol{n}_{p'}} \mathrm{d}S, \tag{2.4}$$

where S_H is the surface of the hydrofoil or propeller blade, duct and hub, S_W the surface of the trailing wake, G Green's function, which is defined as $1/R(p,p')$ in three dimensions and $2lnR(p,p')$ in two dimensions and R the distance between the two points p and p'.

The panel method is based on potential theory, which is inviscid. The effect of viscosity can be taken into account by placing boundary layer sources on the surfaces S_H and S_W, which is known as the viscous/inviscid interaction method. The edge velocity of the boundary layer is from solving the potential flow by using the panel method. The strength of the boundary layer sources can be obtained from a boundary layer solver (Drela 1989) and the viscous velocity on the ith panel is obtained by

$$\boldsymbol{U}_{i,vis} = \boldsymbol{U}_{i,ind} + \sum_{j=1}^{N+N_W} C_{ij}\sigma_j, \tag{2.5}$$

where $\boldsymbol{U}_{i,ind}$ is the edge velocity on the ith panel, N and N_W the number of panels on S_H and S_W, C_{ij} the source influence coefficient matrix and σ_j the boundary layer source strength on the jth panel.

Drela's (1989) model can predict the transition points from the laminar flow to turbulent flow on both the pressure side and the suction side. However, in the presented method, the flow is assumed to be fully turbulent. Forced transitions at 1 % chord length from the leading edge are applied in the VII method throughout this study, and results are compared with fully turbulent RANS simulations.

2.2. *The extension model*

An extension model is needed for sections with blunt TEs because the viscous/inviscid interaction method only applies to sections with sharp TEs. Physically, the extension represents the separated flow downstream of the blunt TE, which is built by quadratic curves to guarantee that both the geometry and the slope are continuous at points A and B, as shown in figure 1. If the coordinates of points A, B and C are given, the extension is uniquely determined by solving the equation set

$$\left.\begin{aligned} y_C &= a_1 x_C^2 + b_1 x_C + c_1 \\ y_A &= a_1 x_A^2 + b_1 x_A + c_1 \\ \text{slope}_A &= 2a_1 x_A + b_1 \\ y_C &= a_2 x_C^2 + b_2 x_C + c_2 \\ y_B &= a_2 x_B^2 + b_2 x_B + c_2 \\ \text{slope}_B &= 2a_2 x_B + b_2 \end{aligned}\right\}, \tag{2.6}$$

where x_A, y_A, x_B, y_B, x_C and y_C are coordinates of points A, B and C, and slope_A and slope_B are known from the original section. The other parameters are the coefficients of the quadratic function and need to be solved.

Equation (2.6) can be written in the rotational invariant form by replacing x and y in the polynomial functions with $r(\theta)$ functions in a polar coordinate system centred around point C. In this case $c_1 = c_2 = 0$ and (2.6) can be simplified as

$$\left.\begin{aligned} \sin(\theta_A) &= a_1 r_A \cos^2(\theta_A) + b_1 \cos(\theta_A) \\ \left.\frac{\mathrm{d}r}{\mathrm{d}\theta}\right|_A &= \frac{\sin^2(\theta_A) + 1 - b_1 \sin(\theta_A)\cos(\theta_A)}{a_1 \cos^3(\theta_A)} \\ \sin(\theta_B) &= a_2 r_B \cos^2(\theta_B) + b_2 \cos(\theta_B) \\ \left.\frac{\mathrm{d}r}{\mathrm{d}\theta}\right|_B &= \frac{\sin^2(\theta_B) + 1 - b_2 \sin(\theta_B)\cos(\theta_B)}{a_2 \cos^3(\theta_B)} \end{aligned}\right\}, \tag{2.7}$$

where r_A, r_B, θ_A and θ_B are known for given points A and B, $\mathrm{d}r/\mathrm{d}\theta|_A$ and $\mathrm{d}r/\mathrm{d}\theta|_B$ from the original geometry.

Points A, B and C are determined in two loops, as shown in the flowchart in figure 2. In the outer loop, an interactive algorithm is used to move points A and B along the surface of the original section until they overlap with the flow separation points, where the skin friction becomes equal to zero with a certain tolerance. In the inner loop, point C is moved in both the horizontal and vertical directions (or in the axial and radial directions for the duct case) by using a two-dimensional Newton–Raphson method. Since there are two unknowns, x_C and y_C, two equations are needed. It is assumed that the pressure is constant in the separated region downstream of the blunt TE, so the force of the extension in the direction perpendicular to the inflow is zero, yielding a zero lift criterion. Similarly, a zero moment criterion requires that the moment around the original TE (point M) is zero, which gives the second equation, as shown in

$$\left.\begin{aligned} \int_{S_E} p(x)\,\mathrm{d}A &= 0 \\ \int_{S_E} p(x) l(x)\,\mathrm{d}A &= 0 \end{aligned}\right\}, \tag{2.8}$$

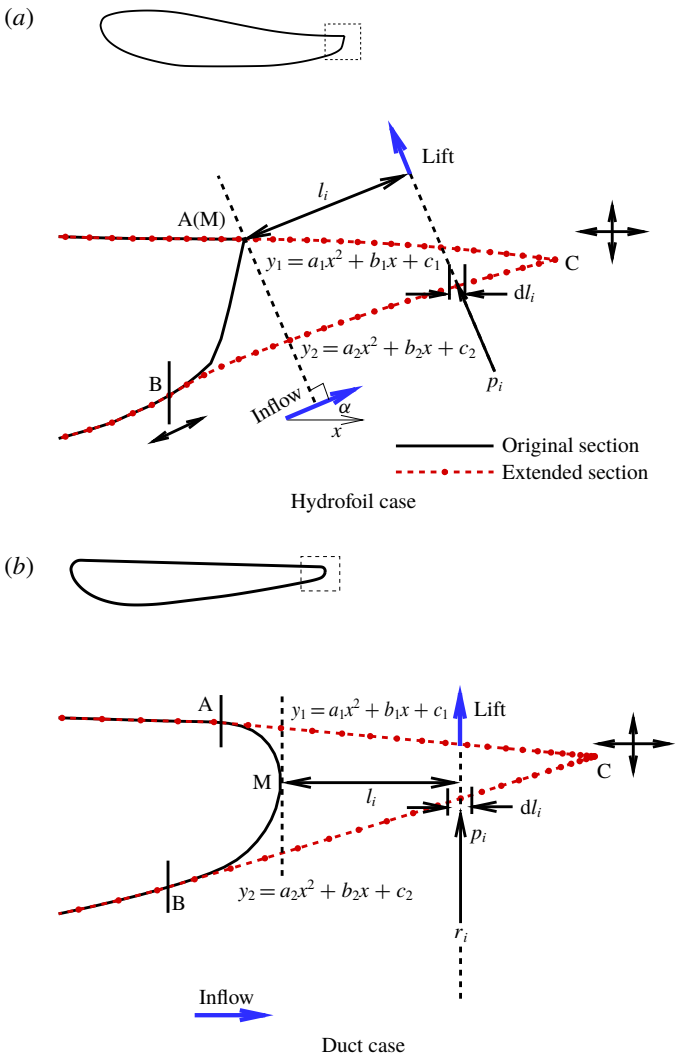

FIGURE 1. (Colour online) A hydrofoil and a duct with blunt TEs, which have been extended to the sharp TEs (points A and B: location where the extended section merges with the original section; point C: TE of the extended section; point M: TE of the original section; l_i: the moment arm from point M to the lift going through the control point of panel i; dl_i: horizontal length of panel i; p_i: pressure at the control point; r_i: radius at the control point; α: angle of attack, exaggerated).

where S_E is the extended surface downstream of the TE (both sides), $p(x)$ the pressure distribution on S_E, $l(x)$ the moment arm from point M with respect to the lift and dA the infinitesimal area in the inflow direction. The discretized form of (2.8) is

$$\left.\begin{aligned} \sum_{lower,upper} \sum_{i} c_{p_i} \times dl_i \times \cos(\alpha) = 0 \\ \sum_{lower,upper} \sum_{i} c_{p_i} \times dl_i \times l_i \times \cos(\alpha) = 0 \end{aligned}\right\} \tag{2.9a}$$

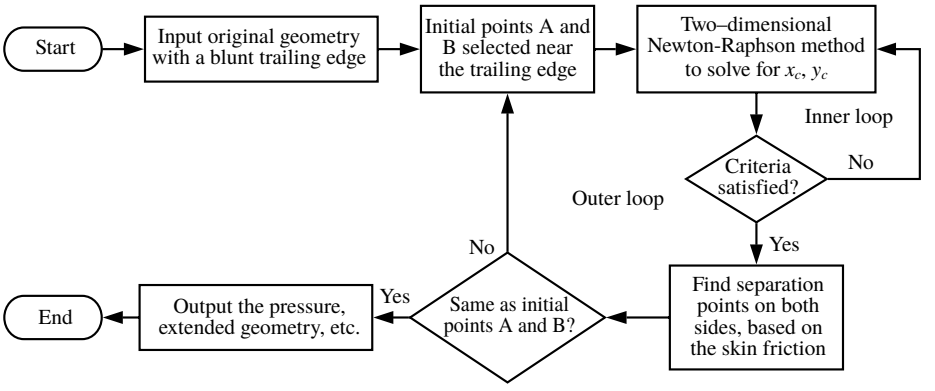

FIGURE 2. Flowchart of the extension model.

and

$$\left.\begin{aligned}\sum_{inner,outer}\sum_{i} c_{p_i}\times \mathrm{d}l_i\times 2\pi r_i = 0\\ \sum_{inner,outer}\sum_{i} c_{p_i}\times \mathrm{d}l_i\times l_i\times 2\pi r_i = 0\end{aligned}\right\} \tag{2.9b}$$

for hydrofoil and duct respectively, where α is the angle of attack, c_{p_i} the pressure coefficient at the control point of panel i, defined as

$$c_{p_i} = \frac{p_i - p_\infty}{\frac{1}{2}\rho v_\infty^2}, \tag{2.10}$$

with p_∞ and v_∞ being the pressure and velocity at far upstream respectively and ρ being the fluid density.

It should be noted that shorter extensions will intrinsically make the force and moment differences between the two sides smaller, thus the Newton–Raphson method tends to converge to smaller x_C. To avoid this drawback, when applying this model numerically, the actual equations used are normalized by setting the pressure coefficient equal to unity in (2.9*b*), as

$$\left.\begin{aligned}\frac{\sum_{lower,upper}\sum_{i} c_{p_i}\times \mathrm{d}l_i\times\cos(\alpha)}{\sum_{lower,upper}\sum_{i} \mathrm{d}l_i\times\cos(\alpha)} = 0\\ \frac{\sum_{lower,upper}\sum_{i} c_{p_i}\times \mathrm{d}l_i\times l_i\times\cos(\alpha)}{\sum_{lower,upper}\sum_{i} \mathrm{d}l_i\times l_i\times\cos(\alpha)} = 0\end{aligned}\right\} \tag{2.11a}$$

and

$$\left.\begin{aligned}\frac{\sum_{inner,outer}\sum_{i} c_{p_i}\times \mathrm{d}l_i \times 2\pi r_i}{\sum_{inner,outer}\sum_{i} \mathrm{d}l_i \times 2\pi r_i} &= 0\\ \frac{\sum_{inner,outer}\sum_{i} c_{p_i}\times \mathrm{d}l_i \times l_i \times 2\pi r_i}{\sum_{inner,outer}\sum_{i} \mathrm{d}l_i \times l_i \times 2\pi r_i} &= 0\end{aligned}\right\}. \tag{2.11b}$$

2.3. *The Reynolds-averaged Navier–Stokes (RANS) method*

In the VII method, the unknown sources and dipoles are placed on the surface of the body and the wake. In the RANS method, the computational domain extends from the body to far upstream and downstream, as shown in figure 3. The velocity field u_i is decomposed into its mean U_i and the fluctuation u_i' (Reynolds 1894), as

$$u_i = U_i + u_i'. \tag{2.12}$$

The governing equations in the RANS method are the continuity equation and the momentum equations, as

$$\nabla \cdot \boldsymbol{u} = 0, \tag{2.13}$$

and

$$\frac{\partial U_i}{\partial t} + U_j \frac{\partial U_i}{\partial x_j} = -\frac{\partial P}{\partial x_i} + \frac{\partial}{\partial x_j}\left(\nu \frac{\partial U_i}{\partial x_j} - \overline{u_i' u_j'}\right), \tag{2.14}$$

where P is the pressure, ν the kinematic viscosity and $\overline{u_i' u_j'}$ the Reynolds stress.

In this study, the results from the flow separation model will be compared with the RANS simulation by using the commercial computational fluid dynamics (CFD) software Ansys-Fluent. The flow is assumed to be incompressible and fully turbulent. At high Reynolds number, there might be vortex shedding after blunt trailing edges, which cannot be predicted by the presented flow separation model and the VII method. However, the focus of this approach is not about the periodic unsteadiness of the vortex shedding, but about the mean pressure and forces on hydrofoils and ducts. Consequently, results from the presented method are compared with the steady RANS simulation, neglecting any vortex shedding. On the other hand, for sections shown in figure 1, the vortex shedding is not strong and its effect is local near the trailing edge, as shown in later sections. The cases with strong vortex shedding and flow separation are beyond the scope of the presented method. In the RANS simulations, the $k-\omega$ *SST* model (Pope 2000) at fully turbulent condition is used, where k is the turbulent kinetic energy, ω is the specific dissipation rate and *SST* is short for the shear stress transport. The detailed numerical settings are listed in table 1. The far-field boundary conditions are velocity inlet and pressure outlet. To make sure that perturbations caused by the foil and duct are not affected by the boundary, the velocity inlet boundaries are 50 times the chord length away from the foil or duct, and the pressure outlet boundaries are 100 times the chord length away, as shown in figure 3.

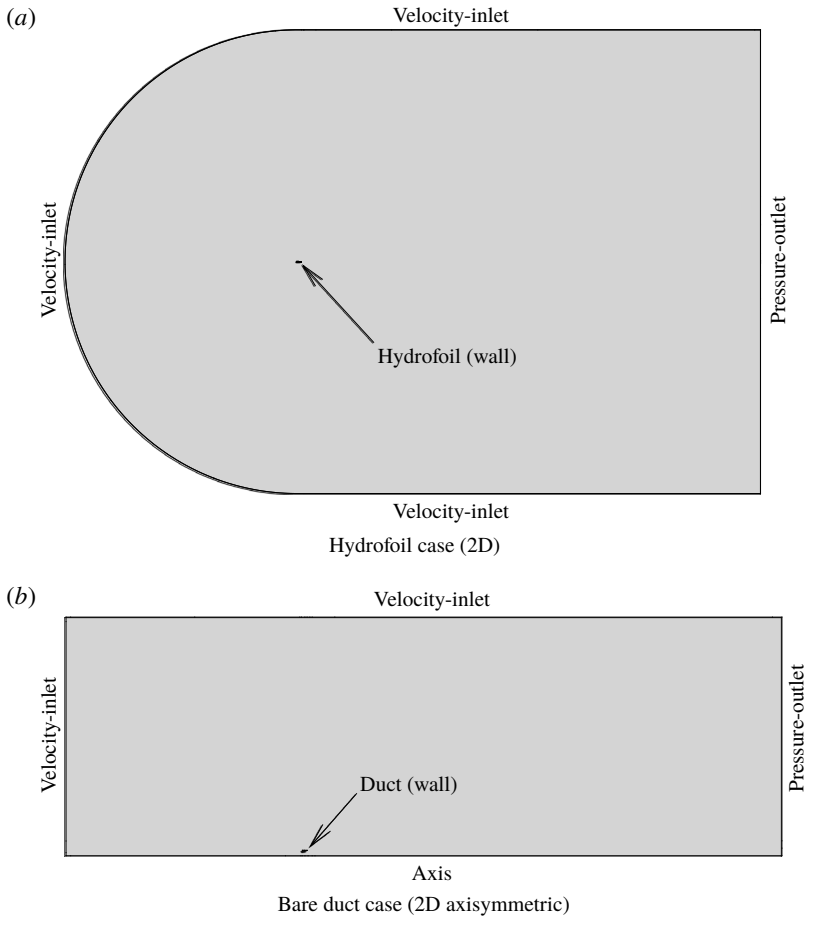

FIGURE 3. The computational domain and boundary conditions in the RANS simulations.

Turbulence modelling	$k-\omega$ *SST* (fully turbulent)
Pressure–velocity coupling scheme	Coupled
Gradient spatial discretization	Least squares cell based
Pressure spatial discretization	Second order
Discretization of momentum, turbulent kinetic energy, specific dissipation rate	Second-order upwind
Residuals	All below 1.0×10^{-6}

TABLE 1. Numerical settings in Ansys-Fluent simulations.

3. Results and discussion

3.1. *The viscous/inviscid interaction method*

In this section, the results from VII are validated with those from the RANS method at fully turbulent conditions of both a hydrofoil and a bare duct with sharp TEs. The validation is necessary because the extension is determined from the pressure

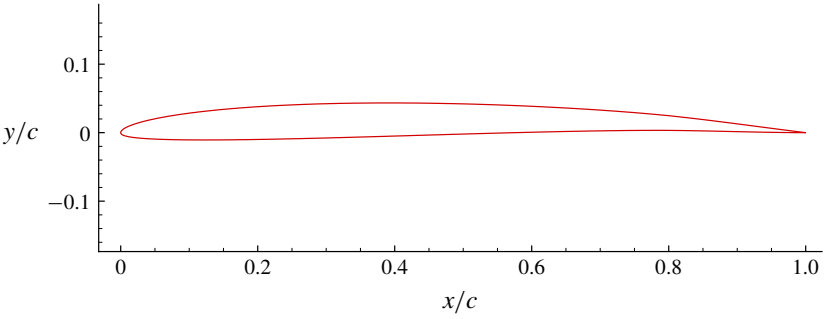

FIGURE 4. (Colour online) A hydrofoil with sharp TE, tested by both VII method and the RANS simulation.

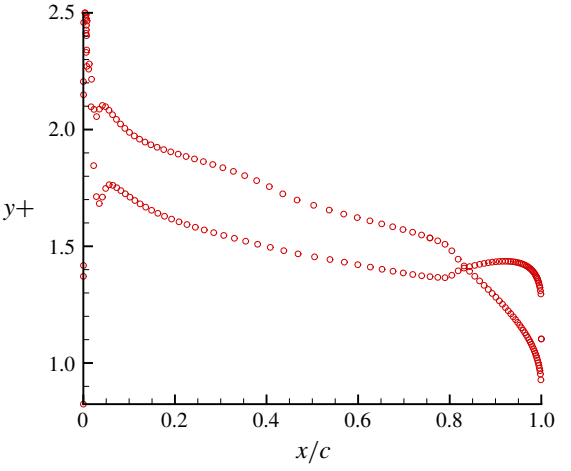

FIGURE 5. (Colour online) Wall $y+$ in the RANS simulation for the hydrofoil with sharp TE.

coefficients and skin friction. In the VII method, the transition locations are forced at 1 % of the chord length from the leading edge. The hydrofoil, as shown in figure 4, has a NACA 0005 thickness distribution and a NACA a = 0.8 mean line with the maximum camber equal to 2 % of the chord length (Abbott & Von Doenhoff 1959). The angle of attack is 1.0°. In the RANS simulation, the total number of quadrilateral cells is 207.6k and the wall distance $y+$ is shown in figure 5. The boundary conditions are the same as shown in figure 3(*a*), and other settings in the RANS simulation are shown in table 1. Compared with the panel method, the VII method improved the correlation with RANS method in pressure predictions, as shown in figure 6(*a*).

The viscous drag coefficient is defined as

$$C_{D,v} = \frac{D}{\frac{1}{2}\rho v_\infty^2 A}, \tag{3.1}$$

where D is the integrated drag force, including the pressure drag and frictional drag in the inflow direction and A is the reference area, taken equal to 1 in the two-dimensional case. Drag in general, due to its small values, is hard to evaluate or

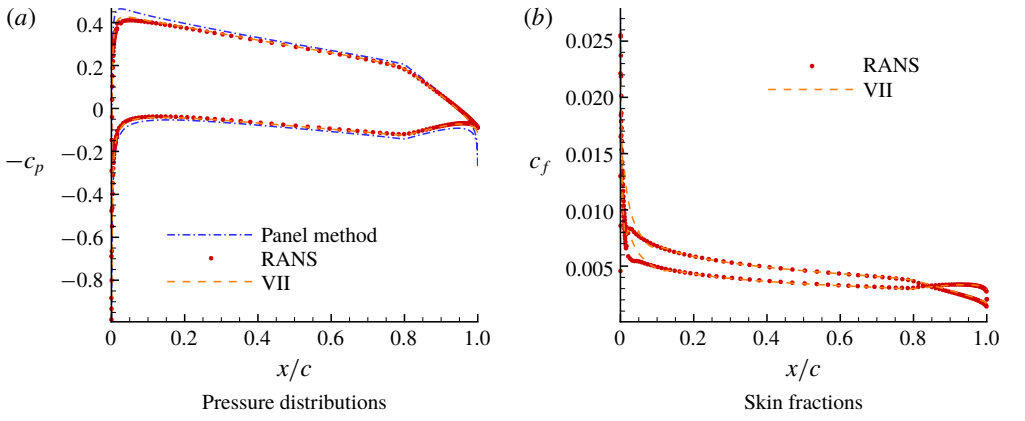

FIGURE 6. (Colour online) The pressure and skin friction predicted from VII agree well with those from RANS for hydrofoil sections with sharp TEs ($Re = 1.0 \times 10^6$, which is defined by the chord length c as $Re = cv_\infty/\nu$; $c_f = \tau_w/(\rho v_\infty^2)/2$, where τ_w is the wall shear stress).

Number of panels (N)	VII	BEM (inviscid)
100	0.00958	0.00025
200	0.00944	0.00005
300	0.00941	0.00002
400	0.00940	0.00001

TABLE 2. Viscous drag coefficients ($C_{D,v}$) predicted by the panel method and the VII method with different numbers of panels (N). Note: $C_{D,v}$ (RANS) = 0.00982.

to measure. The theoretical drag coefficient from the panel method, which is based on the potential theory and fully inviscid, is zero. However, this value is not always zero but a small number, which can be regarded as the numerical integration error, as shown in table 2. Considering that when $N = 200$, the drag coefficient from the panel method is two orders magnitude smaller than those from the VII method, 200 panels are used throughout the presented study in the VII method. Besides, full cosine spacing is adopted, which concentrates more panels near the leading edge and trailing edge in the VII method.

A bare duct means that the interaction between the propeller and the duct is neglected so the problem is simplified to two dimensions, and the axisymmetric sources are used in the boundary layer solver. Duct 19Am is modified from Duct 19A (Kuiper 1992), which has a round TE. The model test of Duct 19Am operating with propeller Ka4-70 was carried out by Bosschers & van der Veeken (2008) to provide validation data for the panel method as it generally does not apply to blunt TEs. Sections of Ducts 19A and 19Am are shown in figure 7(*a*).

In the axisymmetric RANS simulation, the total number of quadrilateral cells is 299.4 k and the $y+$ is smaller than 5 to model the viscous flow accurately in the boundary layer region. Detailed settings of the RANS simulation can be found in table 1. As shown in figures 6(*a*) and 7(*b*), the pressures predicted by the VII method agree well with those from the RANS method in sharp TE sections, and thus can be used confidently in the extension model.

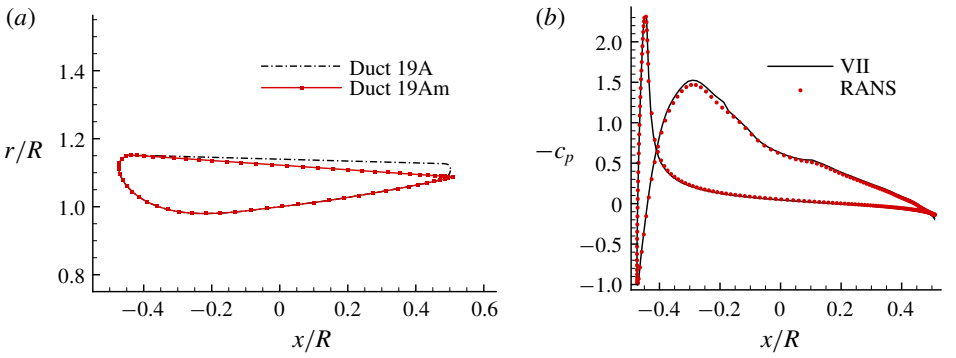

FIGURE 7. (Colour online) The pressure predicted from VII agrees well with that from RANS for bare duct sections with sharp TEs ($Re = 1.0 \times 10^6$, which is defined by the chord length of the duct c as $Re = cv_\infty/\nu$; the lengths are non-dimensionalized by the blade radius R). (*a*) Duct section with a round TE is modified to sharp TE, (*b*) pressure distribution on the bare duct with a sharp TE.

3.2. *Hydrofoil case with a blunt trailing edge*

For the hydrofoil shown in figure 1(*a*), there is flow separation downstream of the blunt TE, as shown in figure 8. This geometry is originally a duct but used as a hydrofoil case in this study to test the extension model. The flow field is from the RANS simulation, in which the total number of quadrilateral cells equals 523.5 k and the $y+$ is smaller than 5. Since there is a sharp corner in the blunt TE (as opposed to round in figure 1*b* and figure 7*a*), the outer loop of the model is applied only on the lower side of the hydrofoil to determine the location of point B. On the upper side, since the geometry at the corner is nearly flat, it is reasonable to start the extension from that location, i.e. point A is fixed at point M. The pressures and skin frictions from the extension model with the VII method are compared with the results from the RANS method for two angles of attack (AOA), as shown in figures 9 and 10. It should be noted that, at different angles of attack, the extended geometries are not the same because the flows around the hydrofoil are different.

3.3. *Bare duct case with a round trailing edge*

The extension model is applied to bare Duct 19A (as shown in figure 7*a*) and the pressure and skin friction on the duct are compared with results from the RANS method for $Re = 1.0 \times 10^6$ and $Re = 1.0 \times 10^7$. Since this duct geometry is built by connecting two straight lines with a round TE, the outer loop of the extension model is not applied as long as points A and B shown in figure 1 do not fall into the round TE part. A good correlation with results from the RANS method can be observed, as shown in figure 11.

Results of the extension model are compared with the steady RANS simulations and the time-averaged pressures and skin frictions are used. To check the effect of the vortex shedding, two unsteady two-dimensional axisymmetric RANS simulations are carried out with different initial conditions. The time size is set as 1.0×10^{-4} s, based on the Courant–Friedrichs–Lewy (CFL) condition. The pressure–velocity coupling scheme is SIMPLEC, and all the other settings are the same as in table 1. In the first unsteady simulation, the flow field of the converged steady run is used as the initial

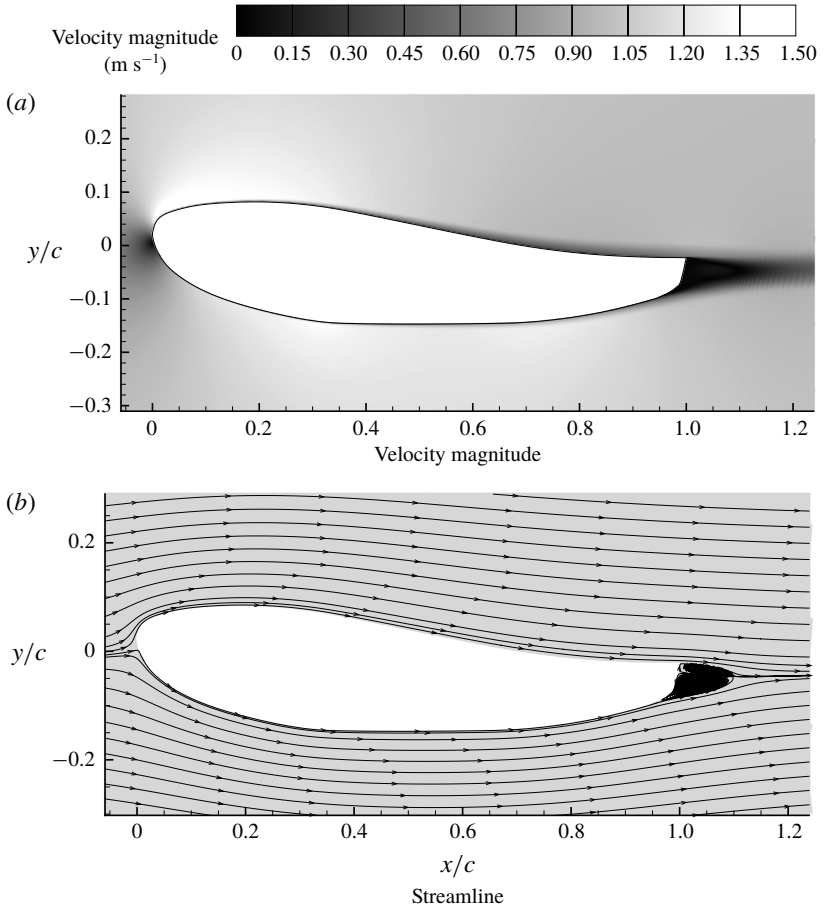

FIGURE 8. Flow separation downstream of a hydrofoil with blunt trailing edge (plotted with zero angle of attack, $\boldsymbol{q}_{in} = 1$ m s^{-1} at far upstream, $Re = 1.0 \times 10^6$; the lengths are non-dimensionalized by the hydrofoil chord length c).

condition, and by comparing the drag coefficient history with the steady simulation, it is shown that there is no vortex shedding and the drag coefficient is equal to that from the steady RANS simulation. In the second unsteady RANS run, the initial flow is set as 1 m s^{-1} everywhere in the domain and the stabilized drag coefficients oscillate within a range of approximately $\pm 5\,\%$ of their mean values, which is approximately $6.8\,\%$ higher than the steady value, as shown in figure 12.

The stabilized streamlines and vorticity are shown in figure 13. To see the effect of the vortex shedding, pressure distributions at two extreme positions in the time history and the time-averaged mean pressure over one period in the unsteady simulation are compared with those from the steady simulation, as shown in figure 14. It is found that even though the drag coefficients at certain initial conditions oscillate with time, its effect on the pressure distributions is local to the trailing edge. Hydrofoils and ducts with strong vortex shedding downstream of the blunt trailing edge cannot be handled by the presented method, therefore are not considered here.

The viscous drag coefficients from the presented method are compared with results from the steady RANS simulations, as shown in table 3. In figure 1, the curve between

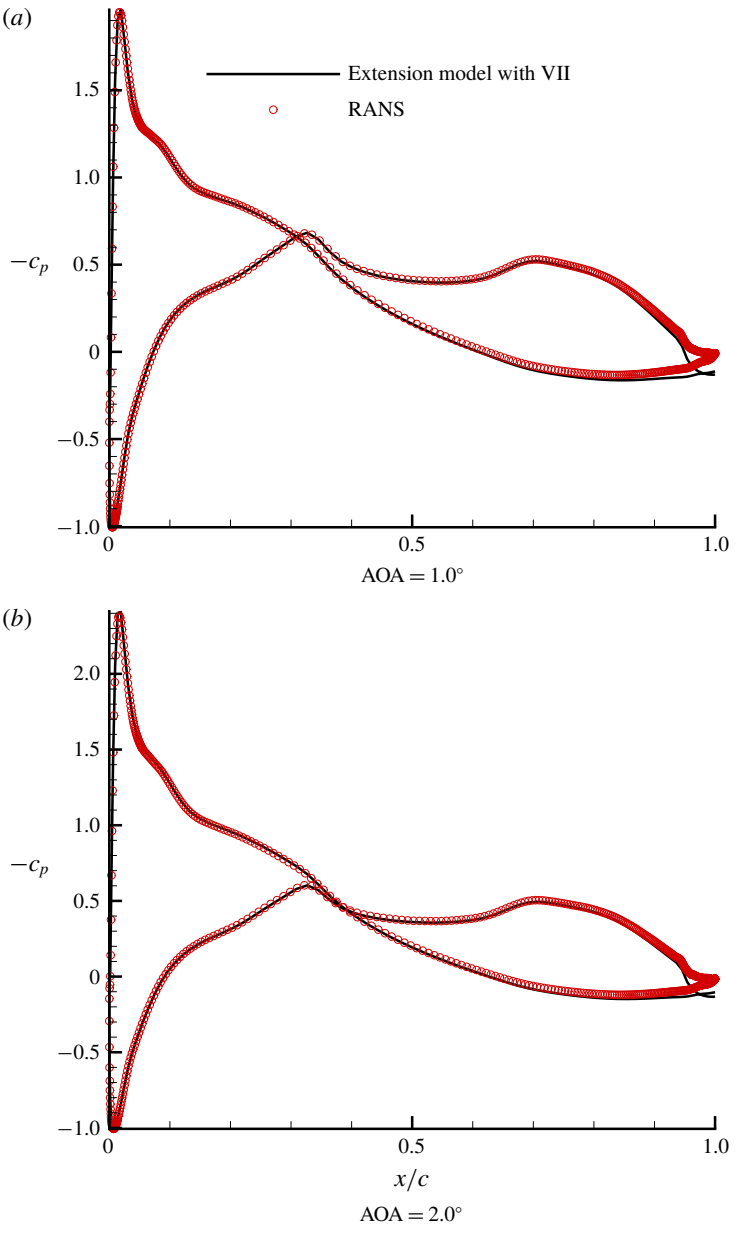

FIGURE 9. (Colour online) The pressure on a hydrofoil with a blunt trailing edge, predicted by the extension model with VII and the RANS method.

point A and point B is replaced by the extension, so c_p and c_f of this part are obtained by interpolation. In the bare duct case, as the Reynolds number increases, the viscous drag coefficients decrease in both methods, as expected.

3.4. *Ducted propeller case with a round trailing edge*

The extension model is applied to Duct 19A working with a square-tip propeller Ka4-70 with zero gap. To see the effect of the presented model, the results are

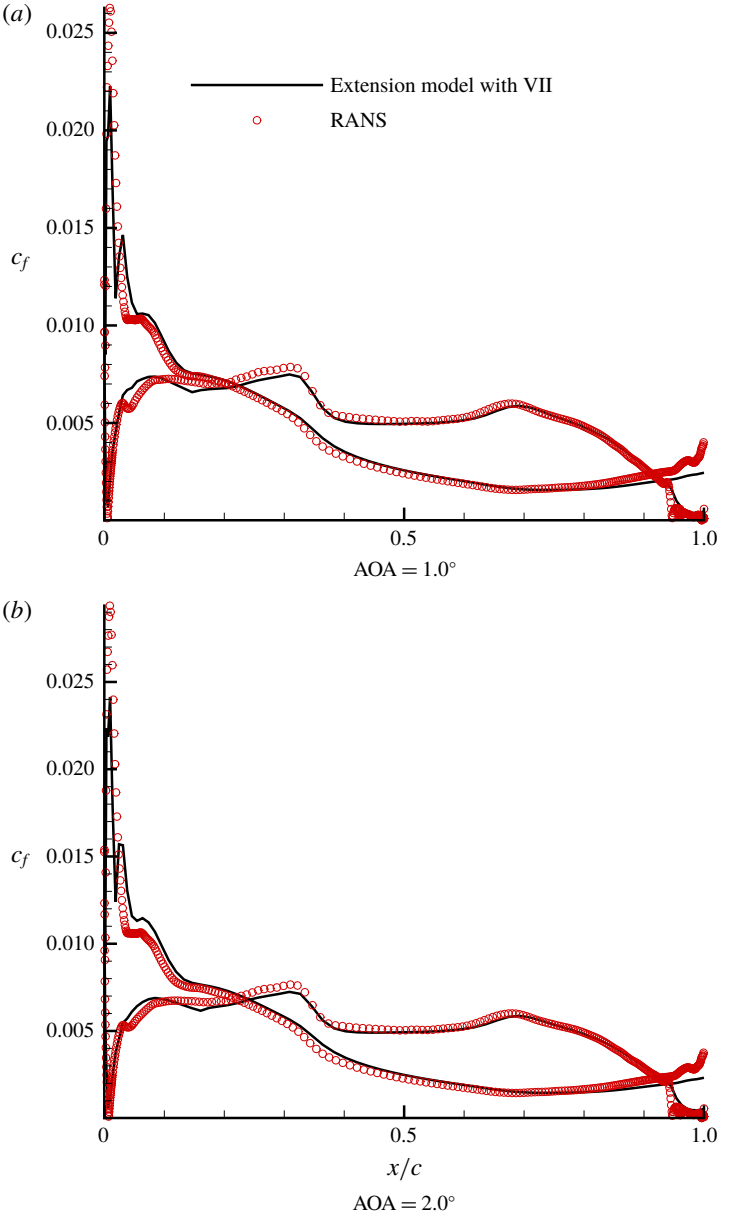

FIGURE 10. (Colour online) The skin frictions on a hydrofoil with a blunt trailing edge, predicted by the extension model with the VII method and the RANS method.

compared with those from an arbitrary extension, as shown in figure 15(*a*). The pressure distribution along the duct when the advanced ratio equals to 0.5 is shown in figure 15(*b*) (averaged in the circumferential direction). The advanced ratio is defined as

$$J = \frac{V_s}{nD}, \tag{3.2}$$

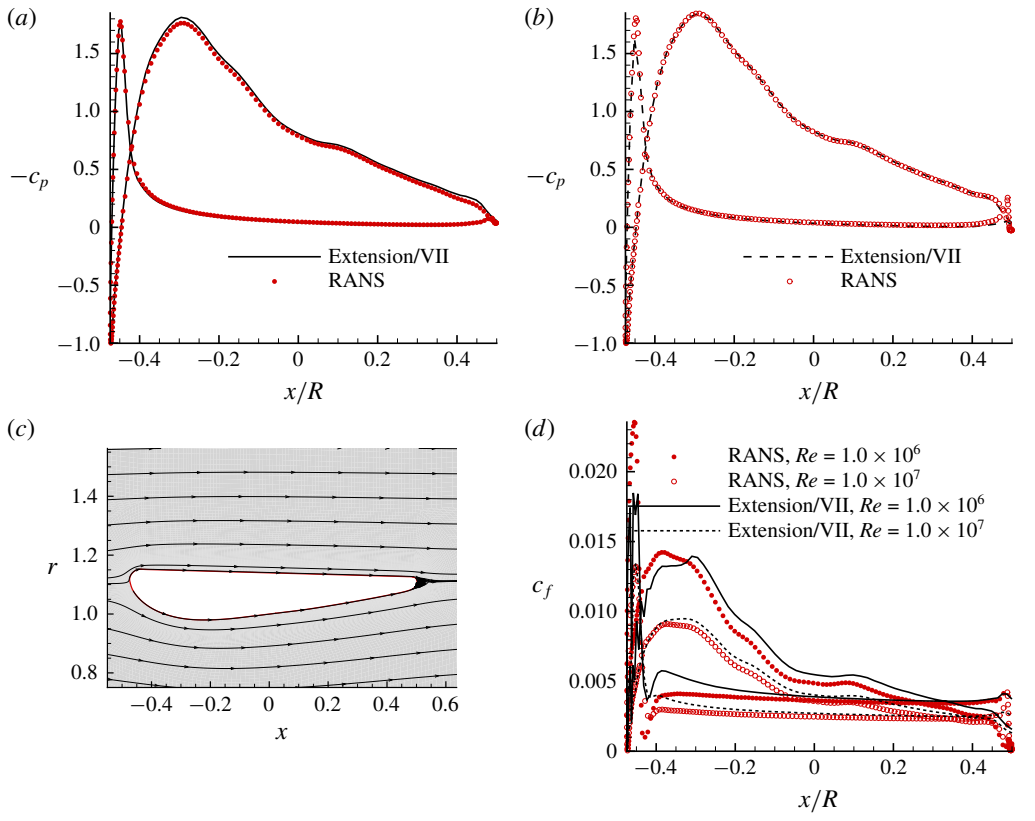

FIGURE 11. (Colour online) The extension model applied to a bare duct with a round trailing edge, and results compared with the RANS method. (*a*) Pressure distribution, $Re = 1.0 \times 10^6$, (*b*) pressure distribution, $Re = 1.0 \times 10^7$, (*c*) streamlines around the duct and the local flow separation after the round TE (predicted by the steady axisymmetric RANS method with $Re = 1.0 \times 10^6$, (*d*) skin friction correlation.

Cases	Hydrofoil		Bare duct	
	AOA = 1.0 deg.	AOA = 2.0 deg.	$Re = 1.0 \times 10^6$	$Re = 1.0 \times 10^7$
RANS	0.02086	0.02113	0.14310	0.09764
Extension/VII	0.01857	0.01906	0.15553	0.10386
Difference	−10.98 %	−9.80 %	8.69 %	6.37 %

TABLE 3. Viscous drag coefficients ($C_{D,v}$) in RANS simulations and the presented method.

where V_s is the ship speed, n the propeller rotational frequency and D the propeller diameter. Note that the pressures at the TE from the arbitrary extension are not equal on both sides. However, in the case that the extension is determined by the present model, the pressures at the TE match with each other, due to the zero lift and zero moment criteria.

The open water characteristics of propeller Ka4-70 operating inside Duct 19A from the extension model are compared with the experimental measurements, as shown in

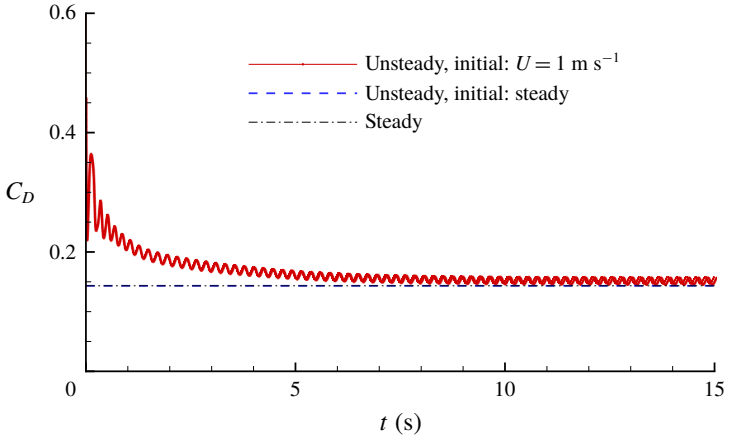

FIGURE 12. (Colour online) Drag coefficient history from the unsteady RANS simulations with different initial conditions, compared with the steady RANS simulation ($Re = 1.0 \times 10^7$).

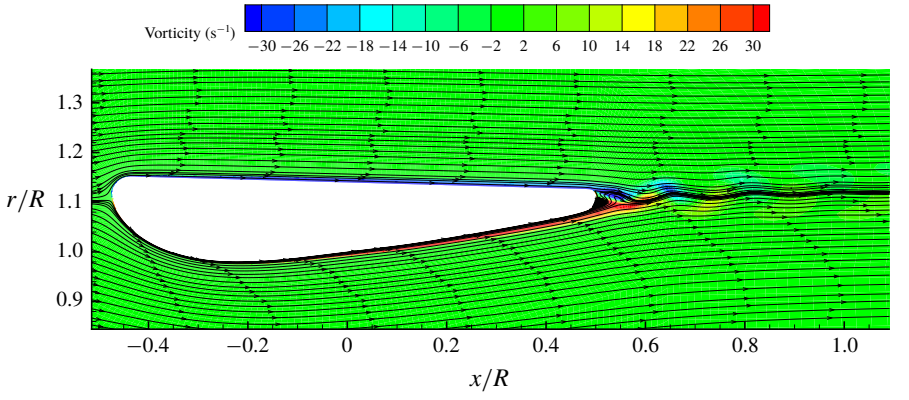

FIGURE 13. (Colour online) Vortex shedding downstream of a bare duct with round TE, predicted by unsteady two-dimensional axisymmetric RANS simulation ($Re = 1.0 \times 10^7$, $t = 15.25$ s, initial condition: $U = 1$ m s^{-1} in the whole domain).

figure 15(*c*). It should be noted that for different advance ratios, the length of the extension zone is not the same because the flows around the duct are different. The thrust coefficient on the propeller is defined as

$$KTP = \frac{T_P}{\rho n^2 D^4}, \tag{3.3}$$

and the thrust coefficient on the duct is defined as

$$KTD = \frac{T_D}{\rho n^2 D^4}, \tag{3.4}$$

where T_P is the thrust on the propeller, T_D the thrust on the duct. The torque coefficient is defined as

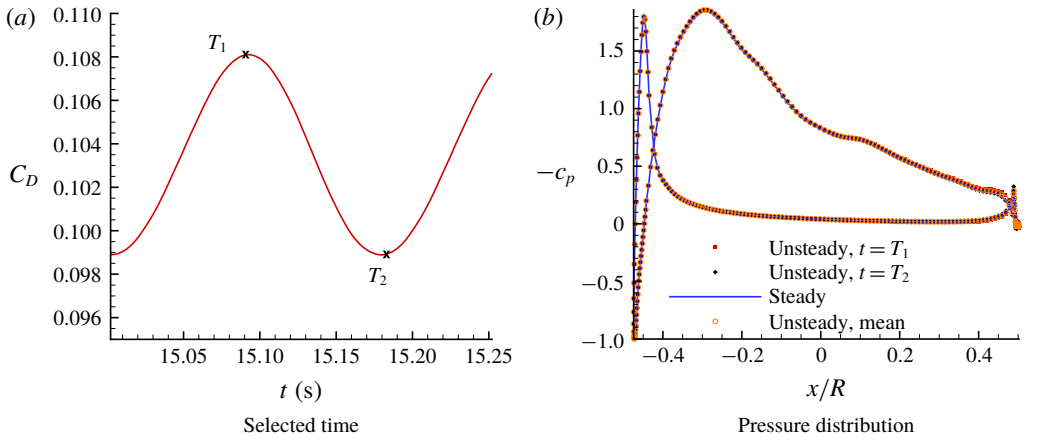

FIGURE 14. (Colour online) The unsteady pressure distributions at two extreme positions in the time history and the time-averaged mean value are all close to results from the steady simulation (bare duct with round TE, $Re = 1.0 \times 10^7$).

$$KQ = \frac{Q}{\rho n^2 D^5}, \tag{3.5}$$

where Q is the torque on the propeller.

In figure 15(*c*), it can be seen that the thrust and torque agree much better with the experimental measurements when the extension zone is determined from the present model rather than by choosing random locations. It should also be noted that the duct trailing edge does not have a strong influence on the thrust from the duct, but has a strong influence on the propeller thrust and torque.

3.5. *Computational efficiency of the extension model*

Compared with the RANS method, this extension model does not require as many computational resources and takes a shorter time in calculation, not to mention the time for pre-processing and post-processing. An overall comparison of the computational efficiency of these two methods is shown in table 4. The RANS simulation for the ducted propeller case was done by Kinnas *et al.* (2015), using an Intel Xeon 2.54 GHz processor. All the other simulations were done on the clusters of the TACC (Texas Advanced Computing Center) using an Intel Xeon E5-2680 2.7 GHz processor. The residuals for all the RANS simulations were set as 1.0×10^{-6}, and only the simulation time was counted.

4. Conclusions

In this paper, an extension model for mean steady flow separation is proposed so that the panel method can be applied to hydrofoils, propellers and ducts with blunt trailing edges. This model uses the criteria of zero lift and zero moment to determine the extension, which physically represents the separated region. This model also adopts an outer loop in an iterative manner to make the locations where the extension starts overlap with the flow separation points where the skin friction becomes equal to zero with a certain tolerance.

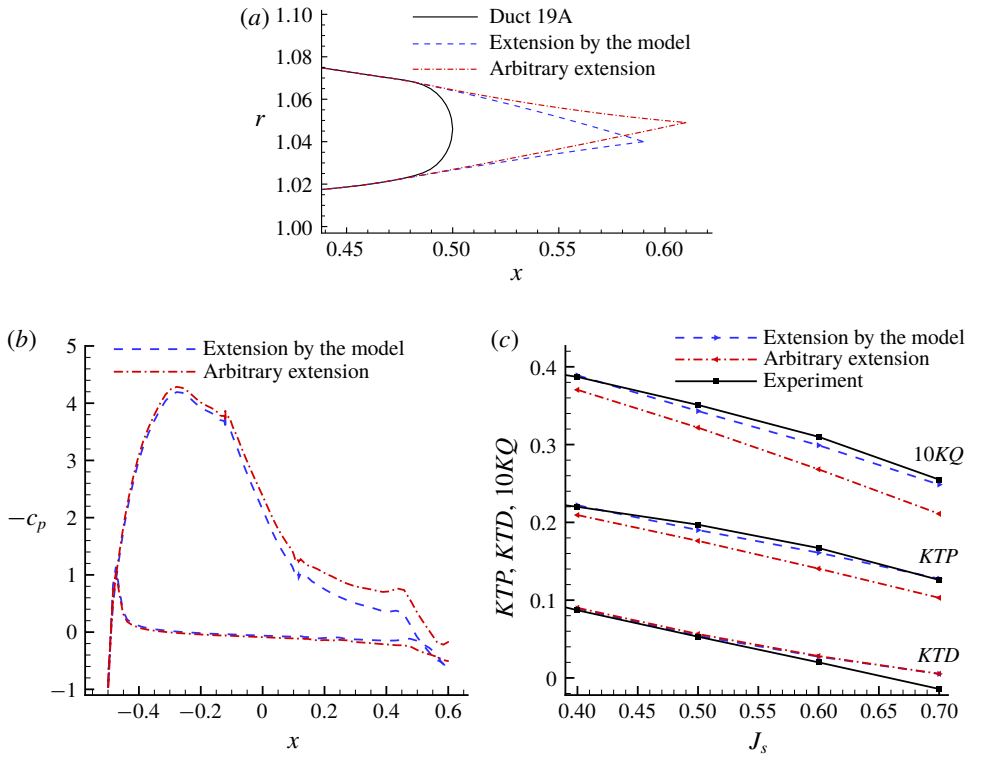

FIGURE 15. (Colour online) The extension model applied to a ducted propeller with a round trailing edge duct (uniform inflow). (*a*) Two extensions for $J = 0.5$, one is from the model and the other is arbitrary, (*b*) pressure distribution on the duct from the two extensions, $J = 0.5$, (*c*) the open water characteristics predicted from the Extension model, arbitrary extension and the experimental measurements.

Cases	Hydrofoil		Bare duct		Ducted propeller
	AOA = 1	AOA = 2	$Re = 1.0 \times 10^6$	$Re = 1.0 \times 10^7$	for each J
RANS	1404 s 16 CPU	984 s 16 CPU	37 s 16 CPU	33 s 16 CPU	> 30 h 32 CPU
Extension model	5 s 1 CPU	4 s 1 CPU	20 s 1 CPU	28 s 1 CPU	3 h to 5 h 16 CPU

TABLE 4. The computational efficiency of the extension model and the RANS method (only the simulation time was counted; the angle of attack is in degrees).

The pressure distribution, skin friction and the open water characteristics from this method correlate well with the results from the steady RANS simulations or with the experimental measurements. Meanwhile, this model requires much fewer computational resources and shorter simulation times. To conclude, this model can serve reliably and efficiently in the design and analysis of hydrofoils and propeller ducts with blunt trailing edges.

Acknowledgements

Support for this research was provided by the US Office of Naval Research (Grant nos. N00014-14-1-0303 and N00014-18-1-2276; K.-H. Kim) partly by Phases VII and VIII of the Consortium on Cavitation Performance of High Speed Propulsors.

REFERENCES

ABBOTT, I. H. & VON DOENHOFF, A. E. 1959 *Theory of Wing Sections, Including a Summary of Airfoil Data*. Courier Corporation.

BALTAZAR, J., FALCÃO DE CAMPOS, J. A. C. & BOSSCHERS, J. 2012 Open-water thrust and torque predictions of a ducted propeller system with a panel method. *Intl J. Rotating Mach.* **2012**, 1–11.

BOSSCHERS, I. J. & VAN DER VEEKEN, R. 2008 Open water tests for propeller Ka4-70 and duct 19A with a sharp trailing edge. *Tech. Rep.* 224457-2-VT. Maritime Research Institute.

BOSSCHERS, J., WILLEMSEN, C., PEDDLE, A. & RIJPKEMA, D. 2015 Analysis of ducted propellers by combining potential flow and RANS methods. In *Proc. 4th Int. Symposium on Marine Propulsors*, pp. 639–648. Institute for Fluid Dynamics and Ship Theory (FDS) – Hamburg University of Technology (TUHH), German Society for Maritime Technology (STG).

DRELA, M. 1989 XFOIL: An analysis and design system for low Reynolds number airfoils. In *Low Reynolds Number Aerodynamics*, pp. 1–12. Springer.

GREENWAY, M. E. & WOOD, C. J. 1973 The effect of a bevelled trailing edge on vortex shedding and vibration. *J. Fluid Mech.* **61** (2), 323–335.

HOEKSTRA, M. 2006 A RANS-based analysis tool for ducted propeller systems in open water condition. *Intl Shipbuild. Prog.* **53** (3), 205–227.

KERWIN, J. E., KEENAN, D. P., BLACK, S. D. & DIGGS, J. G. 1994 A coupled viscous/potential flow design method for wake-adapted, multi-stage, ducted propulsors using generalized geometry. *Trans. Soc. Nav. Archit. Mar. Engrs* **102**, 23–56.

KERWIN, J. E., KINNAS, S. A., LEE, J.-T. & SHIH, W.-Z. 1987 A surface panel method for the hydrodynamic analysis of ducted propellers. In *Transactions of Society of Naval Architects and Marine Engineers*. Society of Naval Architects and Marine Engineers.

KERWIN, J. E. & LEE, C.-S. 1978 Prediction of steady and unsteady marine propeller performance by numerical lifting-surface theory. In *Transactions of Society of Naval Architects and Marine Engineers*. Society of Naval Architects and Marine Engineers.

KIM, S., KINNAS, S. A. & DU, W. 2018 Panel method for ducted propellers with sharp trailing edge duct with fully aligned wake on blade and duct. *J. Mar. Sci. Engng* **6** (3), 1–22.

KINNAS, S. A., FAN, H. & TIAN, Y. 2015 A panel method with a full wake alignment model for the prediction of the performance of ducted propellers. *J. Ship Res.* **59** (4), 246–257.

KINNAS, S. A., LEE, H., SUN, H. & HE, L. 2007 Performance prediction of single or multi-component propulsors using coupled viscous/inviscid methods. In *Proc. 10th Int. Symposium on the Practical Design of Ships and other Floating Structures, Houston, TX*. American Bureau of Shipping.

KUIPER, G. 1992 The Wageningen propeller series. *Tech. Rep.* 92-001. Published on the occasion of the 60th anniversary of the Maritime Research Institute (MRINE).

LEE, H. & KINNAS, S. A. 2006 Prediction of cavitating performance of ducted propellers. In *Proc. 6th Int. Symposium on Cavitation, CAV2006*. Maritime Research Institute Netherlands (MARIN).

MAGI, E. C. & GAI, S. L. 1998 Flow behind castellated blunt-trailing-edge aerofoils at supersonic speeds. *J. Fluid Mech.* **375**, 85–111.

MAJDFAR, S., GHASSEMI, H., FOROUZAN, H. & ASHRAFI, A. 2017 Hydrodynamic prediction of the ducted propeller by CFD solver. *J. Mar. Sci. Technol.* **25** (3), 268–275.

MOULIJN, J. 2015 Application of various computational methods to predict the performance and cavitation of ducted propellers. In *Proc. 4th Int. Symposium on Marine Propulsors*, vol. 15, p. 31. Institute for Fluid Dynamics and Ship Theory (FDS) – Hamburg University of Technology (TUHH), German Society for Maritime Technology (STG).

PAN, Y. & KINNAS, S. A. 2011 A viscous/inviscid interactive approach for the prediction of performance of hydrofoils and propellers with nonzero trailing edge thickness. *J. Ship Res.* **55** (1), 45–63.

PARK, H., LEE, D., JEON, W.-P., HAHN, S., KIM, J., KIM, J., CHOI, J. & CHOI, H. 2006 Drag reduction in flow over a two-dimensional bluff body with a blunt trailing edge using a new passive device. *J. Fluid Mech.* **563**, 389–414.

POPE, S. B. 2000 *Turbulent Flows*. Cambridge University Press.

REYNOLDS, O. 1894 On the dynamical theory of incompressible viscous fluids and the determination of the criterion. *Phil. Trans. R. Soc. Lond. Ser.* A **186**, 123–164.

SERVINI, P., SMITH, F. T. & ROTHMAYER, A. P. 2017 The impact of static and dynamic roughness elements on flow separation. *J. Fluid Mech.* **830**, 35–62.

SU, Y. & KINNAS, S. A. 2017 A generalized potential/RANS interactive method for the prediction of propulsor performance. *J. Ship Res.* **61** (4), 214–229.

SURANA, A., GRUNBERG, O. & HALLER, G. 2006 Exact theory of three-dimensional flow separation. Part 1. Steady separation. *J. Fluid Mech.* **564**, 57–103.

TIAN, Y. & KINNAS, S. A. 2012 A wake model for the prediction of propeller performance at low advance ratios. *Intl J. Rotating Mach.* **2012**, 1–11.